Available online at www.sciencedirect.com
SCIENCE DIRECT®
Journal of Nuclear Materials 344 (2005) 1–7
journal of nuclear materials
www.elsevier.com/locate/jnucmat

Highlights of experimental thermodynamics in the field of nuclear fuel development

Heiko Kleykamp *

Forschungszentrum Karlsruhe, Institut für Materialforschung I, Postfach 3640, 76021 Karlsruhe, Germany

Abstract

Results of basic thermodynamic studies are presented in the fields of oxide fuel pins and their alloys with fission products and of the neutron multiplier beryllium. Gibbs energy of formation measurements of solid phases using galvanic cells with CaF_2 electrolyte are exemplarily described for chromium carbides, URu_3 and URh_3. The calculation of the corresponding value of UPd_3 is demonstrated using the phase diagram of the U–Pd–Sn system. The phase behaviour of $(U,Pu)O_2$ in a steady-state temperature gradient between the solidus and the liquidus is explained. The $O/(U + Pu)$ redistribution in a temperature gradient is measured which allows the calculation of the heat of transport of the oxygen vacancies. The obstacles for measurements of the enthalpies of transformation and melting of beryllium are commented, the temperatures are only 14 degrees apart from each other below melting at 1283 °C. The high enthalpy of transformation is interpreted by the compressed *c*/*a*-axis ratio of the hcp modification.

1. Introduction

Thermodynamic studies on nuclear materials are presented which were conducted within the fast breeder, nuclear safety and nuclear fusion programs of Forschungszentrum Karlsruhe and were published earlier in the open literature stating full particulars. The highlights are recapitulated on the occasion of this conference which include more recent investigations of oxide fuels and alloys with fission products and of the neutron multiplier beryllium.

2. Gibbs energies of formation

Gibbs energies of formation of intermetallic compounds, alloys with broad homogeneity ranges and ceramic phases can be easily obtained by emf measurements with galvanic cells of the second type using solid electrolytes, e.g., $Zr(Y)O_2$, ThO_2, CaF_2, etc. The design of a cell is presented in Fig. 1. The quartz holding devices shield the thermocouple and confine the cell: the light electrolyte pellet is surrounded with the dark electrodes on both sides; the bright rhenium pellets protect the electrodes from incompatibilities of the platiunum–rhodium leads. An example is given by the measurement of the Gibbs energy of formation $\Delta_f G^\circ$ of Cr_3C_2 [1]:

$$(-)Cr, CrF_2|CaF_2|CrF_2, Cr_3C_2, C(+) \quad (1)$$

The positive electrode on the right-hand side is the working electrode representing a coupled equilibrium with the auxiliary electrolyte CrF_2. As Cr forms fluorides with several Cr valencies, the ternary Cr–C–F system has to be worked out first in order to establish the fluoride in equilibrium with the Cr_3C_2–C couple.

* Tel.: +49 7247 822888; fax: +49 7247 824567.
E-mail address: heiko.kleykamp@imf.fzk.de

0022-3115/$ - see front matter © 2005 Elsevier B.V. All rights reserved.
doi:10.1016/j.jnucmat.2005.04.006

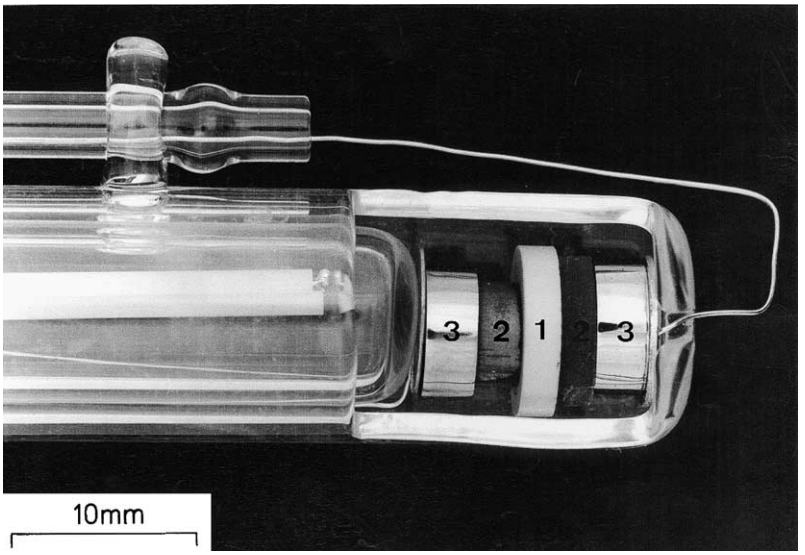

Fig. 1. Design of a galvanic cell arranged between two quartz tubes. The solid electrolyte (1) is located in the centre of the pellet stack, surrounded by the electrodes (2) and the rhenium buffers (3). The platinum–rhodium disks and leads are connected with an electrometer. The thermocouple tip is located within the inner quartz tube.

This necessary action is sometimes disregarded in the literature. The virtual left-hand and right-hand electrode reactions are

$$\text{left:}\quad 3Cr + 6F^- = 3CrF_2 + 6e^- \tag{2a}$$

$$\text{right:}\quad 6e^- + 3CrF_2 + 2C = Cr_3C_2 + 6F^- \tag{2b}$$

which result in the gross reaction and the corresponding thermochemical equation for the Gibbs energy of reaction $\Delta_r G^\circ$, resp.,

$$3Cr + 2C = Cr_3C_2 \tag{3}$$

$$\Delta_r G^\circ = 6\mathbf{F}E = \Delta_f G^\circ < Cr_3C_2 > \tag{4}$$

The constant **F** is the Faraday number. The measured emf E is essentially the difference of the logarithms of the fluorine partial pressures on both sides of the galvanic cell. The quantity $\Delta_f G^\circ$ of Cr_3C_2 is obtained without any further thermodynamic data. Similarly, the Gibbs energies of formation of Cr_7C_3 and $Cr_{23}C_6$ have been obtained by this method. These results are important for rating the formation of chromium carbides in the steel claddings [1].

The fission platinum metals Ru, Rh and Pd, together with the fission products Mo and Tc, form quinary hexagonal phases [2] which appear as metallic inclusions in irradiated $(U,Pu)O_2$ fuels. If a fast breeder pin becomes defected during irradiation the entering sodium coolant reduces the fuel into its hypostoichiometric state. The consequences are a strong decrease of the oxygen partial pressure as well as the formation of $Na_3(U,Pu)O_4$ and intermetallic fcc $(U_xPu_{1-x})Rh_3$ and $(U_{1-x}Pu_x)Pd_4$ compounds and Sn rich Pu–Pd–Rh phases. This occurs by a coupled reduction of the fuel according to the simplified reaction scheme

$$\begin{aligned}(U,Pu)O_2 + Mo,Tc,Ru,Rh,Pd + Na \\ \rightarrow (U,Pu)O_{2-x} + Mo,Tc,Ru + (U,Pu)\cdot(Rh,Pd)_{3+x} \\ + Na_3(U,Pu)O_4\end{aligned} \tag{5}$$

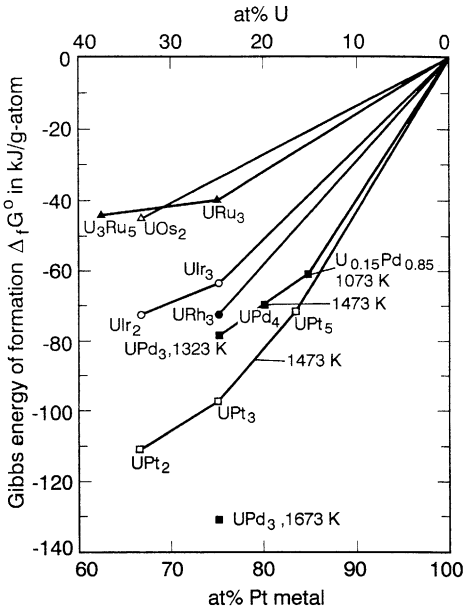

Fig. 2. Gibbs energies of formation of uranium–platinum metal phases at 1100 K unless otherwise stated.

The reaction is facilitated by the very high stability of these actinide–platinum metal phases (Fig. 2). However, Ru is not in the position to form this type of phases because the thermodynamic stability of URu_3 is too low, which can be recognized by the phase-field partitioning of the respective phase diagrams of the U–F–platinum metal systems. Fig. 3 illustrates the difference of the thermodynamic stability of URu_3 and URh_3 by the different phase-field partitioning of the U–Ru–F and U–Rh–F systems. URh_3 is more stable than URu_3. Therefore, the binary URh_3–Rh system is in equilibrium with UF_4 that has a lower U activity than UF_3 in equilibrium with the binary URu_3–Ru system. Hence, the galvanic cells for measurements of the Gibbs energies of formation of URu_3 and URh_3 are [3]

$$(-)\mathrm{U}, \mathrm{UF_3}|\mathrm{CaF_2}|\mathrm{UF_3}, \mathrm{URu_3}, \mathrm{Ru}(+) \quad (6)$$

$$(-)\mathrm{UF_3}, \mathrm{UF_4}|\mathrm{CaF_2}|\mathrm{UF_4}, \mathrm{URh_3}, \mathrm{Rh}(+) \quad (7)$$

In the Pd rich range of the U–Pd system, the UPd_3 and UPd_4 phases occur [4]. As the U solubility in Pd is high, emf measurements in this system are more difficult. However, the calculation of the Gibbs energy of formation of $TiNi_3$-type UPd_3 is possible by knowledge of the thermodynamic data of UPd_4 [5] and of $SnPd_2$ and $SnPd_3$ [6] as well as the phase-field partitioning of the ternary U–Pd–Sn system (Fig. 4). The thermodynamic data in point P of Fig. 4 can be then calculated assuming an ideal solid solution of the $SnPd_3$–UPd_4 system. As the thermodynamic activities are constant in the three-phase field P–Q–R, the Gibbs energy of formation can be approximately calculated which gives $\Delta_f G^\circ \langle \mathrm{UPd_3} \rangle = -78$ kJ/g-atom at 1323 K [4].

3. Phase studies in a temperature gradient

In the following, the phase behaviour of $(\mathrm{U,Pu})O_2$ is discussed under a steady-state temperature gradient. UO_2 and PuO_2 are completely miscible in the solid and the liquid. When, e.g., a $U_{0.8}Pu_{0.2}O_2$ solid solution is heated to a temperature between the solidus, 2720 °C , and the liquidus, 2780 °C , according to the updated pseudobinary phase diagram [7], coexisting solid and liquid phases are formed. The liquid is richer in PuO_2 than the solid. A single-phase melt exists above the liquidus. When the mixed oxide is rapidly heated to the two-phase region and a steady-state temperature gradient is attained in the fuel between the melting temperatures of UO_2 and PuO_2, at first a solid–liquid two-phase region is formed containing UO_2 rich solid particles in a PuO_2 rich melt. However, the position of these solid particles is unstable under the temperature gradient. Their UO_2 richer hot sides are dissolved in the melt and UO_2 resolidifies on their cold sides in a manner that the entire particles move to the solid phase boundary which becomes richer in UO_2. The two-phase field disappears rapidly (Figs. 5 and 6). The discontinuous UO_2 and PuO_2 concentrations must fulfill the conditions of identical chemical potentials of UO_2 and PuO_2 at the phase boundary between the solid and the liquid phase around 2750 °C . The concentrations are 16% PuO_2 in the solid and 25% PuO_2 in the liquid according to the phase diagram of the UO_2–PuO_2 system. The course of the UO_2 concentration is complementary [8]. The discontinuity of concentration at the phase boundary and the disappearance of the two-phase field hold in general for binary systems with complete solubilities of the components.

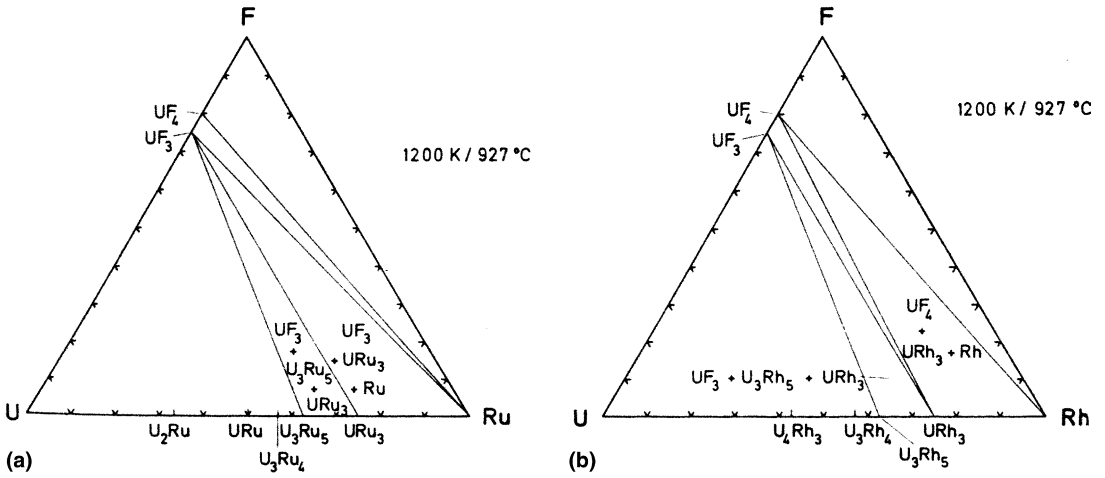

Fig. 3. Isothermal sections of the U–Ru–F (a) and U–Rh–F (b) systems indicating the different phase-field partitioning due to the higher thermodynamic stability of URh_3 than that of URu_3.

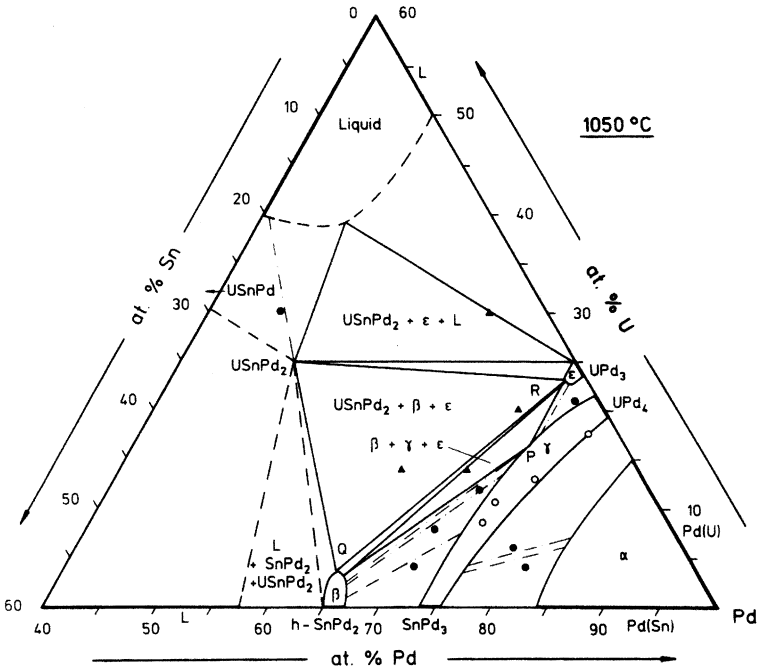

Fig. 4. Isothermal section of the Pd rich range of the U–Pd–Sn system at 1050 °C.

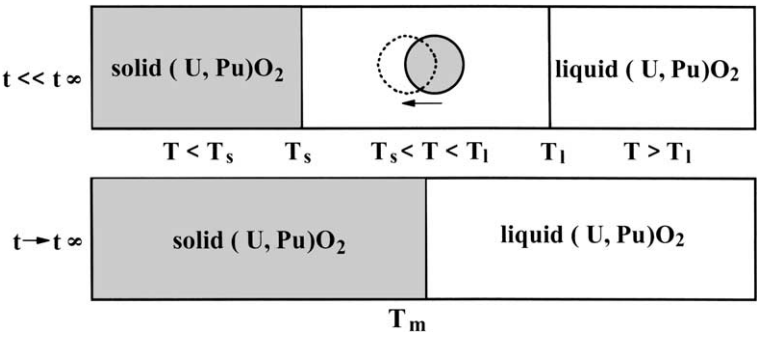

Fig. 5. Model of solid $(U,Pu)O_2$ transport in a steady-state temperature gradient. The UO_2 richer solid particles with higher melting points move within the two-phase solid–liquid region between the liquidus T_l and solidus T_s to lower temperatures and form at the end one common phase boundary.

We have observed dark borders in fuel pins of power-to-melt irradiations within our mild transient operation program [9]. The solid–liquid border is not visible in the etched axial microstructure, however, it is detectable in the α-autoradiograph superposed to the microstructure [8]. The high flux of the α-particles from the Pu decay, which has a short half-life compared to the U decay, whitens the positive of the α-autoradiograph. The narrow dark concentric ring in the α-autoradiograph of a fuel pin cross-section points to the Pu depleted solid–liquid boundary of the fuel [9]. Quantitative X-ray microanalysis of Pu and U in Fig. 6 confirms the Pu decrease on the solid side of the phase boundary at 0.43 of the relative fuel radius. This gives 15% PuO_2 and 85% UO_2 [8]. These concentrations correspond to an interface temperature of 2750 °C according to the UO_2–PuO_2 phase diagram.

A severe redistribution phenomenon of oxygen is observed in the temperature gradient of hypostoichiometric mixed oxide $(U,Pu)O_{2-x}$ which is enabled by intrinsic defects in the anion sublattice. This phenomenon was investigated and explained years ago by Schumacher et al. [10]. As the analytical techniques of the oxygen analysis in micro-areas were recently improved we have directly measured the radial oxygen concentration profile of short-time irradiated $U_{0.8}Pu_{0.2}O_{1.95}$. A

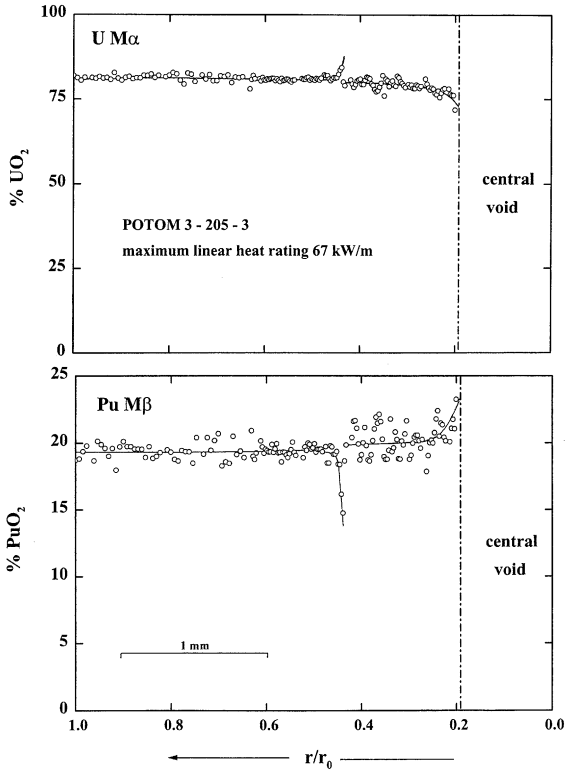

Fig. 6. UO_2 and PuO_2 concentrations in a $U_{0.8}Pu_{0.2}O_{2-x}$ fuel pin under a steady-state temperature gradient as a function of the relative fuel radius r/r_0. The solid–liquid phase boundary is located at 0.43 r_0.

synthetic Ni–C multilayer device was utilized for the registration of the oxygen Kα line by X-ray microanalysis [11]. The radial profile given in Fig. 7 yields an O/M ratio of 2.00 at the fuel pellet surface and an O/M ratio

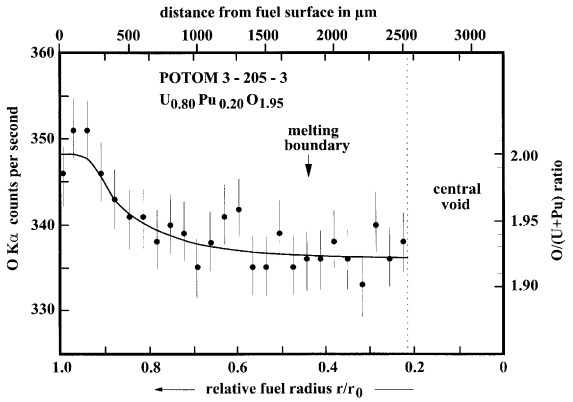

Fig. 7. Oxygen concentration in a short-time irradiated $U_{0.8}Pu_{0.2}O_{1.95}$ fuel pin as a function of the relative fuel radius r/r_0.

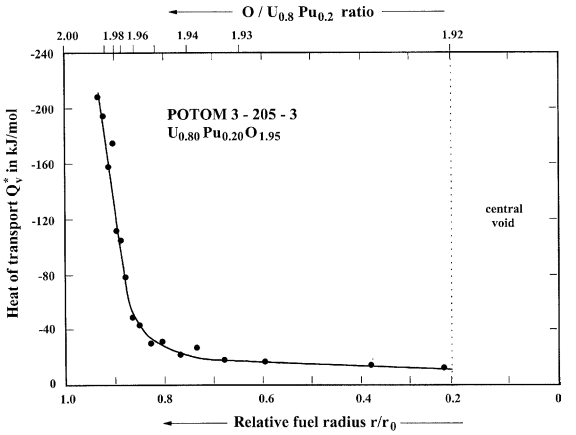

Fig. 8. Heat of transport Q_v^* of oxygen vacancies in a short-time irradiated $U_{0.8}Pu_{0.2}O_{1.95}$ fuel pin as a function of the relative fuel radius r/r_0.

of 1.92 with a nearly horizontal tangent at the central void. The oxygen concentration gradient is controlled by the oxygen vacancy flux in direction to higher temperatures. The profile can quantify the heat of transport Q_v^* of oxygen vacancies using the transport equation [10]. It is presented as a function of the relative fuel radius in Fig. 8 [8]. The heat of transport is negative, has its minimum value on the fuel surface, and tends to zero by a horizontal tangent at the central void of the fuel pin. As the heat of transport is negative the oxygen vacancy flow is directed to the high-temperature region. The flow of oxygen vacancies is brought to a standstill when the ratio of $O/U_{0.8}Pu_{0.2} \approx 1.92$ is reached.

4. High-temperature calorimetry

In the calorimetry section, some more difficult experiments are discussed on toxic beryllium by DTA and calorimetry at high temperatures when vapours can be produced. Beryllium is used as a neutron multiplier in fission and fusion reactors. The metal has a transition from the hcp to the bcc modification only 14 degrees below the melting temperature. The transition was detected in the year 1949. We could separate the two peaks by DTA without any interference because the time constant of the instrument is very low [12]. However, the heat of transformation and the heat of melting were shown to be of the same order of magnitude which is quite unusual. High-temperature calorimetry resulted indeed in similar latent heats. The heat of transformation is $\Delta_{tr}H = (6100 \pm 500)$ J/mol, and the heat of melting is $\Delta_m H = (7200 \pm 500)$ J/mol [12]. An on-line result is given in Fig. 9. The heat of transformation of beryllium is higher than that of other elements transforming from the hcp to the bcc crystal structure with increasing

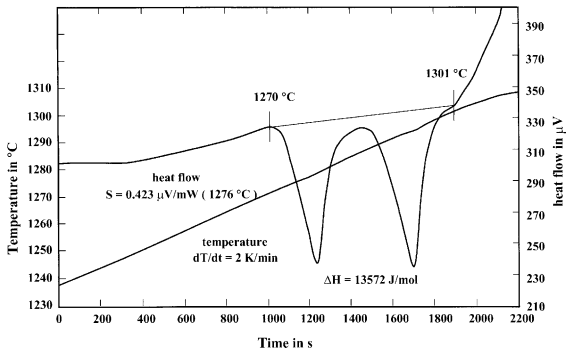

Fig. 9. Enthalpy of transformation and melting of beryllium by anisothermal calorimetry resulting in averaged $\Delta_{tr}H = 6.1$ kJ/mol and $\Delta_{m}H = 7.2$ kJ/mol, respectively.

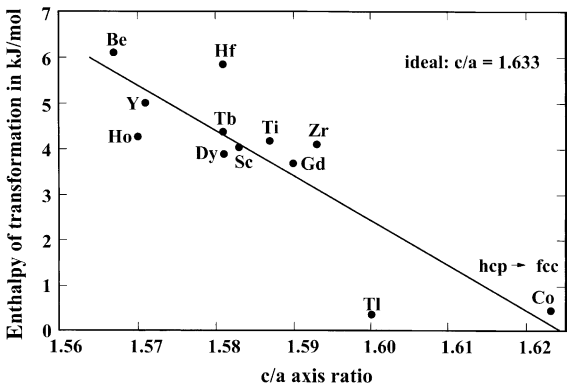

Fig. 10. Enthalpy of the hcp–bcc transformation of metals as a function of the c/a-axis ratio of their hcp modification. The hcp–fcc transformation of Co is given for comparison. The straight line is the result of a least-squares fit.

temperature [13]. This can be explained by the very compressed c/a-axis ratio of beryllium with $c/a = 1.567$ compared to the ideal ratio $c/a = 1.633$. The enthalpy of transformation of elements plotted as a function of the c/a-axis ratio in Fig. 10 shows the influence of stronger deviations of this ratio from the ideal ratio [14]. This can be explained as follows: The energy of stretching of the c-axis to the ideal c/a-ratio is the major part of the enthalpy of transformation. On the other hand, the energy of transforming the ideal hcp lattice in first co-ordination by destroying the arrangement of the nearest neighbours and re-arrangement of the new bcc lattice with a different co-ordination number is low.

5. Summary and conclusion

A review was given of own experimental work on the thermodynamics of materials used particularly in the nuclear fields. The methods of Gibbs energy of formation measurements were presented on carbides and alloys by galvanic cells with solid CaF_2 electrolyte. The calculation of thermodynamic data of binary compounds using experimental results of phase diagrams of suitable ternary systems were exemplified. Redistribution phenomena of binary phases in a steady-state temperature gradient were discussed. High-temperature calorimetry studies by the heat flux method were illustrated. The results were selected from numerous experiments performed within the fast breeder, the nuclear safety and the nuclear fusion programs of Forschungszentrum Karlsruhe.

There are urgent needs to continue experimental thermodynamic work at high temperatures in the fields of fuels and breeding materials for fission and fusion reactors. This includes thermodynamics and phase equilibria in the very important U–Pu–O system and the corresponding oxide and nitride systems of the so-called minor actinides, lithium breeding ceramics and liquid alloys, beryllium compounds, alloys for accelerator driven systems (ADS), such as Pb–Bi, and last but not least the broad field of the thermodynamics of fission product systems [15].

The equipment in thermochemistry and analytical chemistry is now fully developed, is easy to operate and offers a synergetic effect in data production and deeper insights into a general perspective. Quite apart of this, in many cases only easy systems have been studied lately. The trend goes even towards duplicating earlier investigations. What is the use of doing again what has already been done? The answer is that further experimental work must have been done since many essential crucial topics remain unsolved.

References

[1] H. Kleykamp, J. Alloys Compd. 321 (2001) 138.
[2] H. Kleykamp, J.O.A. Paschoal, R. Pejsa, F. Thümmler, J. Nucl. Mater. 130 (1985) 426.
[3] H. Kleykamp, Pure Appl. Chem.. 63 (1991) 1401.
[4] H. Kleykamp, S.G. Kang, J. Nucl. Mater. 230 (1996) 280.
[5] S. Möbius, L. Hellwig, C. Keller, J. Less-Common Met. 121 (1986) 43.
[6] H.J. Schaller, H. Brodowsky, Z. Metallk. 69 (1978) 87.
[7] Y. Philipponeau, Melting point of U, Pu mixed oxide fuels, in: Fast reactor European collaboration data sheet, AEA Technology, Windscale, 1990, unpublished.
[8] H. Kleykamp, J. Nucl. Mater. 294 (2001) 8.
[9] D. Freund, D. Geithoff, H. Steiner, J. Nucl. Mater. 204 (1993) 228.
[10] M. Bober, G. Schumacher, Adv. Nucl. Sci. Technol. 7 (1973) 121;
C. Sari, G. Schumacher, J. Nucl. Mater. 61 (1976) 192.

[11] H. Kleykamp, in: Beiträge zur elektronenmikroskopischen Direktabbildung von Oberflächen vol. 22, 1989, p. 133.
[12] H. Kleykamp, Thermochim. Acta 345 (2000) 179; Netsu Sokutei 27 (2000) 100.
[13] A.T. Dinsdale, SGTE data for pure elements, NPL report DMA (A) 195 (1989).
[14] H. Kleykamp, J. Nucl. Mater. 294 (2001) 88.
[15] R.A. Verrall, J. Nucl. Mater. 294 (2001) VII.